Published in final edited form as:
J Exp Biol. 2019 May 8; 222(Pt 9): . doi:10.1242/jeb.185488.

Avian surface reconstruction in free flight with application to flight stability analysis of a barn owl and peregrine falcon

Nicholas E. Durston[1], **Xue Wan**[2,3], **Jian G. Liu**[2], and **Shane P. Windsor**[1,*]

[1]Department of Aerospace Engineering, University of Bristol, Queen's Building, University Walk, Bristol BS8 1TR, UK

[2]Department of Earth Science and Engineering, Imperial College London, South Kensington Campus, London SW7 2AZ, UK

[3]Key Laboratory of Space Utilization, Technology and Engineering Center for Space Utilization, Chinese Academy of Sciences, Beijing, 100094, China

Abstract

Birds primarily create and control the forces necessary for flight through changing the shape and orientation of their wings and tail. Their wing geometry is characterised by complex variation in parameters such as camber, twist, sweep and dihedral. To characterise this complexity, a multi-view stereo-photogrammetry setup was developed for accurately measuring surface geometry in high resolution during free flight. The natural patterning of the birds was used as the basis for phase correlation-based image matching, allowing indoor or outdoor use while being non-intrusive for the birds. The accuracy of the method was quantified and shown to be sufficient for characterising the geometric parameters of interest, but with a reduction in accuracy close to the wing edge and in some localised regions. To demonstrate the method's utility, surface reconstructions are presented for a barn owl (*Tyto alba*) and peregrine falcon (*Falco peregrinus*) during three instants of gliding flight per bird. The barn owl flew with a consistent geometry, with positive wing camber and longitudinal anhedral. Based on flight dynamics theory, this suggests it was longitudinally statically unstable during these flights. The peregrine falcon flew with a consistent glide angle, but at a range of air speeds with varying geometry. Unlike the barn owl, its glide configuration did not provide a clear indication of longitudinal static stability/instability. Aspects of the geometries adopted by both birds appeared to be related to control corrections and

[*]Author for correspondence (shane.windsor@bristol.ac.uk).
iDN.E.D., 0000-0002-4621-9468
X.W., 0000-0002-0659-2559
J.G.L., 0000-0002-3090-0152
S.P.W., 0000-0002-7597-4497

Competing interests
The authors declare no competing or financial interests.

Author contributions
Conceptualization: N.E.D., S.P.W.; Methodology: N.E.D., X.W., J.G.L., S.P.W.; Software: N.E.D., X.W., J.G.L.; Validation: N.E.D., X.W.; Formal analysis: N.E.D., S.P.W.; Investigation: N.E.D., S.P.W.; Resources: J.G.L., S.P.W.; Data curation: N.E.D.; Writing - original draft: N.E.D.; Writing - review & editing: N.E.D., X.W., J.G.L., S.P.W.; Visualization: N.E.D.; Supervision: J.G.L., S.P.W.; Project administration: N.E.D., S.P.W.; Funding acquisition: S.P.W.

Data availability
The original images used in this study have been deposited in the Dryad Digital Repository (Durston et al., 2019): dryad.sf755pr

this method would be well suited for future investigations in this area, as well as for other quantitative studies into avian flight dynamics.

Keywords

Bird flight; Stereo-photogrammetry; Flight dynamics; Flight control; Wing geometry; *Tyto alba*; *Falco peregrinus*

Europe PMC Funders Author Manuscripts

Introduction

Birds primarily generate the forces required to support and control their flight by changing the shape and orientation of their wings and tail. As aerodynamic forces are often highly sensitive to subtle changes in geometry, accurate high-resolution measurements of geometry are desirable for quantifying bird flight control and aerodynamic performance. Measurements based on narcotised birds or dead specimens do not accurately capture the wing shape used in flight because of the inability of the bird to respond to the flow conditions. For example, comparison between the measured wing cross-sections of a pigeon (*Columba livia*) when freely flying and narcotised revealed significant differences in aerofoil shape and twist distribution (Biesel et al., 1985). With dead birds, the effects of tissue desiccation and correct limb positioning also need to be considered. This has motivated the development of methods for directly measuring the wing geometry of freely flying birds.

Most methods developed for measuring wing shape in flight are based on the use of visual imagery. Stereo-photogrammetry with manual point matching has been used in a number of previous studies. The dorsal wing surface of a house sparrow (*Passer domesticus*) was reconstructed from ~100 points measured during flight in a wind tunnel (Bilo, 1971, 1972; Bilo and Nachtigall, 1985). This approach was later combined with wing thickness measurements from narcotised birds to enable reconstruction of 10 aerofoil sections from a gliding pigeon (Biesel et al., 1985; Butz et al., 1985). The dorsal and ventral surfaces of a starling (*Sturnus vulgaris*) gliding in a wind tunnel were measured using several stereo camera pairs, revealing distinct differences in wing geometry at different flow velocities (Brill et al., 1989). Multi-station photogrammetry with manual point matching was used to reconstruct the arm wing of a perching steppe eagle (*Aquila nipalensis*) based on ~250 points (Carruthers et al., 2010). A similar high-speed camera setup with a manual line matching approach was also used to reconstruct the feather shafts and outline of a flapping hummingbird wing (Maeda et al., 2017). Recently, two approaches with significantly higher spatial resolution (~10^4 points) have been developed. In the first, a moving camera, multi-view stereo-photogrammetry arrangement along with a projected random dot pattern was used with automated point matching based on normalised cross-correlation. This approach allowed the reconstruction of a single wing of a barn owl (*Tyto alba*) at 1 kHz temporal resolution, revealing the complex variation in wing camber, twist and thickness during a complete flap cycle (Wolf and Konrath, 2015). In the second, the deformation of a structured light pattern filmed by a single camera was used to automatically reconstruct the dorsal surface of both wings of a pacific parrotlet (*Forpus coelestis*) in flapping flight at 3.2 kHz (Deetjen et al., 2017). A limitation of the manual methods of point matching is that it is

difficult to obtain high-resolution measurements of the entire surface because of the need to match distinct recognisable features by eye. While the approaches using projected light overcome this by using computational image-processing techniques to identify patterns projected onto the bird, this requires the bird to fly in a small imaging volume with carefully controlled lighting conditions.

In this paper, a method for making high-resolution surface geometry measurements of flying birds is presented. The main novelty of this method is the use of phase correlation-based image matching applied to the naturally occurring texture patterns of the feathers. As such, this approach does not require markers on the bird or projected light patterns. Data can be obtained outdoors or indoors with minimal infrastructure and used to image a relatively large volume while being non-intrusive for the birds. A detailed description of the method is provided, including accuracy assessment. The utility of this novel method and the results it can produce are then illustrated in the context of assessing flight stability and control of a free-gliding barn owl, *Tyto alba* (Scopoli 1769), and a peregrine falcon, *Falco peregrinus* Tunstall 1771.

Stability theory

Generating sufficient force to support weight is clearly important for flight, but equally important is the ability to control the aerodynamic forces that are generated in order to maintain a desired flight trajectory. While the first aspect has been relatively well studied in birds, the second aspect looking at how birds control their flight has not received as much attention (Thomas and Taylor, 2001). One of the first steps required to understand bird flight control is to characterise the stability of the geometries the birds use in flight, which in turn determines the degree of correction that they need to make to control their flight. Based on the in-flight measurements made using the novel method presented here, the flight stability of the geometries adopted by the two birds will be analysed in the context of existing flight dynamics theory.

The main factor determining the controllability of an aircraft or gliding bird is its inherent stability. An inherently stable configuration will eventually return to its equilibrium condition (forces and moments sum to zero) following a disturbance. With an unstable configuration, disturbances from equilibrium require active control, either from the pilot or from the automatic flight control system, to ensure steady flight (Etkin and Reid, 1996). Because of their tendency to depart from equilibrium, unstable configurations exhibit greater manoeuvrability, which is why many combat aircraft are designed to be unstable (Cook, 1997). Unlike most aircraft, however, birds can make large changes in the area, relative position, orientation and shape of their wings and tail, and may be able to adjust their degree of stability to suit different flight modes and/or for manoeuvre control (Taylor, 2005; Thomas and Taylor, 2001). For example, an unstable configuration, with its enhanced manoeuvrability, might be desirable when attacking prey in mid-air, while a more stable configuration might reduce energy consumption during long-distance soaring by reducing the control motions required. These suggestions remain speculative, however, as the stability of the numerous flight configurations adopted by birds is yet to be quantified (Taylor, 2005; Tobalske, 2007).

In flight dynamics, aircraft are normally treated as rigid bodies with three rectilinear (forward, lateral, vertical) and three rotational (roll, pitch, yaw) degrees-of-freedom. Longitudinal (forward, vertical, pitch) motion is often modelled separately from lateral–directional (lateral, roll, yaw) motion as the longitudinal dynamics are relatively uncoupled from the lateral dynamics. Here, we will concentrate on longitudinal static stability as there are aspects of this that can be inferred from geometry. Static stability refers to the initial direction of the system's response towards, or away from, equilibrium, while dynamic stability refers to the damping of oscillations over time. Analysis of dynamic stability requires more knowledge of the systems dynamics than can be inferred from geometry, so is beyond the scope of the present analysis. Similarly, the link between lateral dynamics and geometry is less well defined and as such will not be discussed here.

A bird or aircraft is longitudinally statically stable when its pitching moment slope is negative at equilibrium:

$$\frac{\partial M}{\partial \alpha} < 0, \quad (1)$$

where M is pitching moment and α is angle of attack (AoA). This condition is shown in Fig. 1A and shows that a disturbance causing an increase in AoA (nose-up) results in a restorative nose-down pitching moment and vice versa. The equivalent case for an unstable system is shown in Fig. 1B, where a pitch disturbance is accelerated by the positive moment slope.

In order to fly steadily (i.e. trimmed flight), there must exist some AoA, α_{trim}, at which both forces and moments sum to zero (i.e. equilibrium). If the moment slopes in Fig. 1A,B were translated to the left, so that their intersection with the horizontal axis became negative, trim would be impossible. This is because there would be no AoA at which both the total vertical force and pitching moment could simultaneously be zero, noting that the origin is at α_0, which is the zero-lift AoA. Assuming a linear moment slope, it is therefore necessary that for stable, trimmed flight:

$$M_0 > 0, \quad (2)$$

where M_0 is the zero-lift pitching moment. As the opposite applies to an unstable configuration, some qualitative assessment of longitudinal static stability is possible, based not on the position of the centre of mass, as is traditionally done for aircraft (Etkin and Reid, 1996), but on the combined contributions of various geometric features to the zero-lift pitching moment. Thomas and Taylor (2001) used this reasoning to predict the geometric features that might be observed in longitudinally statically stable gliding birds and these predictions will be used here to explore whether stability may be inferred from the morphologies measured in flight.

Fig. 1C–J shows different geometric features that generate positive (Fig. 1C,E,G,I) or negative (Fig. 1D,F,H,J) zero-lift pitching moments. These geometric features can therefore

be considered as indicators of longitudinal static stability or instability if their collective contribution to the zero-lift pitching moment is clear. A cambered aerofoil generates a pitching moment which can be considered to act at approximately 25% chord (M_{AC}) and to be constant with changes in α (Anderson, 2007; Thomas and Taylor, 2001). A negatively cambered aerofoil produces a nose-up pitching moment (Fig. 1C), while a positively cambered aerofoil produces a nose-down pitching moment (Fig. 1D). In conventional aircraft, negative camber is almost never used because it is aerodynamically inefficient (i.e. large lift-to-drag penalty). However, symmetric or reflex cambered aerofoils are sometimes used that eliminate or minimise the nose-down zero-lift pitching moment (Nickel and Wohlfahrt, 1994).

The drag of the wing (D) contributes towards the zero-lift pitching moment depending on the relative vertical positions of the centre of drag and the centre of mass. With a high wing configuration, wing drag contributes a nose-up zero-lift pitching moment (Fig. 1E) and vice versa for a low wing configuration (Fig. 1F).

Combining aft sweep with wash-out (twisting the wing to reduce α along the span) generates a nose-up zero-lift pitching moment (Fig. 1G) through the spanwise distribution of lift (L), and is often used in tailless aircraft (Nickel and Wohlfahrt, 1994). Forward sweep and wash-in (twisting the wing to increase α along the span) would also achieve the same effect (not shown). Aft-sweep and wash-in generate a nose-down zero-lift pitching moment (Fig. 1H), and again, forward sweep with wash-out would have the same effect (not shown).

A horizontal tail plane is commonly used in conventional aircraft to generate the nose-up zero-lift pitching moment required for a stable configuration (Fig. 1I). In this case, the zero-lift AoA of the tail is negative relative to the zero-lift AoA of the wing, which is known as longitudinal dihedral (Etkin and Reid, 1996). Unstable configurations may require the opposite, referred to here as longitudinal anhedral (Fig. 1J). Note that having longitudinal dihedral does not necessarily imply that the tail generates negative lift at the trim AoA.

Overall, the features shown only provide a clear indication of longitudinal static stability if their combined contribution to zero-lift pitching moment is obviously positive or negative. For example, a combination of aft sweep, wash-out and longitudinal dihedral would be a strong indicator of stability. Conversely, aft sweep, wash-in and longitudinal anhedral would represent a strong indicator of instability. If the geometric indicators are mixed, then longitudinal static stability cannot be easily inferred with this approach and further aerodynamic analysis would be required.

This geometric assessment of longitudinal static stability is based on the assumption of a linear moment slope and does not require any knowledge of the anteroposterior (fore–aft) position of the centre of mass, as is used in the traditional analysis of aircraft longitudinal stability (Etkin and Reid, 1996). The zero-lift pitching moment is a pure couple and as such does not change with the anteroposterior position of the centre of mass, as can been appreciated by considering the effect of its position on the configurations shown in Fig. 1C–J. The assumption of a linear pitching moment slope is a standard one for subsonic aircraft operating below stall (Cook, 1997), but this analysis still holds if this assumption is relaxed

to the more general assumption that the pitching moment slope does not change sign over the range α_0 to α_{trim}. The pitching moment of a flying bird has not been directly measured, but measurements on an isolated bird wing showed the positive linear pitching moment slope expected for a positively cambered wing when measured about a point posterior to the quarter chord (Withers, 1981).

In this analysis, it is also assumed that the bird is a rigid body, meaning that the geometry could be rotated to a different AoA without changing shape. This analysis does not assume that the bird does not actually actively change its geometry when flying at lower AoA, just that the geometry measured at equilibrium could conceptually be rotated to an angle where zero lift would be produced. The stability characteristics of the system for small perturbations about the equilibrium condition are then inferred. These assumptions are the same as those used in standard linear flight dynamics analysis (Cook, 1997). Overall, this analysis does not require knowledge of the location of the centre of mass, which is difficult to determine for a flying bird, and allows directional inferences about longitudinal static stability to be made based on measured in-flight geometry.

Materials and Methods

Experimental animals and field conditions

A 1 year old adult female barn owl and a 3 year old adult male peregrine falcon were used in this study. The birds were trained falconry birds and were owned, housed and trained by professional falconers and were very familiar with performing flights on cue in front of cameras. All work was approved by the University of Bristol Animal Welfare and Ethical Review Body (UIN UB/14/049). The flights were conducted outdoors in a large open field in order to promote flight that was as natural as possible, as well as to provide sufficient space for the birds to reach a steady glide, with the peregrine falcon in particular requiring a long flight path (~60 m) before initiating gliding flight.

The birds were flown over 2 days. The first day was used to iteratively adjust the positions of the start and end points of the birds' flights to ensure reliable glides through the measurement volume. The barn owl flew between the gloves of two bird trainers spaced approximately 18 m apart on flat level ground and would glide for several metres prior to initiating its perch sequence. The peregrine falcon would only glide given a significantly longer flight path of approximately 60 m, taking off from an elevated take-off position situated on a 3 m high mound on the edge of the level field. The peregrine falcon flew to a lure placed on a table where it landed at relatively high speed compared with the barn owl. The distance between the centre of the measurement volume and the landing point was approximately 4 m for the barn owl and 9 m for the peregrine falcon.

Flights took place in summer during dry weather and light winds (Beaufort scale <~2), with the birds flying into the prevailing wind direction to encourage gliding behaviour. A 1.2 m high plastic mesh fence was erected prior to the measurement volume to ensure the birds were more than a wingspan in height above the ground and therefore out of ground effect (Anderson, 1999). After the first day, the barn owl reliably glided past the camera setup on a highly repeatable trajectory. In contrast, the peregrine falcon's speed and trajectory varied

between flights, even though it consistently flew on demand. All data were collected on the second day of flying. The barn owl completed 10 flights while the peregrine falcon completed 24 flights. As the barn owl flew very consistently, three representative flights (referred to as O1, O2 and O3) with the highest image quality were selected for analysis. Only three of the 24 peregrine flights (referred to as P1, P2 and P3) were suitable for analysis because of variation in its position and reduced light levels later in the day.

Experimental setup

The experimental setup consisted of eight digital single lens reflex photographic cameras (70D, Canon, Tokyo, Japan) arranged in pairs above and below the expected flight path (Fig. 2). Two camera pairs were mounted on a 4.7 m-high mobile access tower to image the bird's dorsal surface, while the other two pairs were placed level with the ground looking up at the bird's ventral surface. Each camera pair had a baseline (distance between the optical centres of the cameras) of approximately 230 mm, with the bird at a range of 2–3 m. Variable focal length lenses (17–50 mm f2.8 XR Di II VC, Tamron, Tokyo, Japan) allowed the field of view to be adjusted depending on the consistency of the flight paths. The focal lengths used were approximately 30 mm for cameras 1–4 (dorsal view) and 17 mm for cameras 5–8 (ventral view), with the bird taking up approximately 0.2 megapixels of the 20 megapixel sensor area (Fig. S1). This small area provided a spatial resolution of approximately 1 point per mm^2 and allowed the exposure to be increased without introducing motion blur, as well as keeping the bird close to the centre of the image where lens distortion was minimised. The cameras were electronically synchronised to within ~1 ms using a commercially available system (Time Control™/Camera Control™ digital systems, Digital Air, Geneva, Switzerland), ensuring any change in the bird's shape was negligible between the images. Any variation in the time of image capture between cameras (<1 ms) may have been due to subtle variations in the mechanics of the cameras rather than the electronic synchronisation signal. The cameras were triggered manually when the bird was at the centre of the measurement volume.

Calibration of the measurement volume was undertaken immediately after the bird flights. A minimum of 40 images of a handheld 300 mm square rigid board with an array of 196 circular reference points was obtained for each camera pair, with locations covering the full extent of the measurement volume. An additional calibration was carried out using a custom-made wand with two 50 mm diameter spheres whose centres were spaced 529.2 mm apart, in order to generate calibration images that could be seen by all cameras simultaneously. Again, a minimum of 40 images were taken, distributed evenly around the measurement volume.

Video cameras (Lumix DFZ400, Panasonic, Osaka, Japan, and GoPro Hero 3+, GoPro Inc., San Mateo, CA, USA) running at 100 frames s^{-1} with resolutions of 1280×720 pixels and 1280×960 pixels, respectively, were positioned either side of the flight path. The GoPro camera was placed on the scaffold tower with the wide-angle lens providing video footage of each flight from a range of approximately 2 m. The Lumix camera was located in the field and was oriented towards the camera setup for capturing flight behaviour several metres before and after the measurement volume. The footage was used for the qualitative

assessment of each flight and estimation of the birds' ground velocity. The latter was estimated using the measured position and orientation of the Lumix camera relative to the stereo pairs and the bird, with the assumption that the bird was flying parallel to the *x*-axis of its wing–body coordinate system. Given the known relative positions and orientations of the bird, stereo pairs and video camera, it was then possible to estimate the distance travelled between frames to obtain the average ground velocity across the measurement volume. A 3-axis sonic anemometer (HS-50, Gill, Lymington, UK, wind speed error <1% rms) sampling at 4 Hz was placed approximately 6 m from the centre of the measurement volume and was used to record the local wind velocity for 2.5 s before and after each set of flight images were captured. The wind and ground velocity estimates were then used to estimate the true air speed, angle of attack and angle of sideslip in each flight (Fig. S1), with the mean and standard deviation for these estimates based on the measured variation in wind velocity.

Analysis procedure

Overview—Stereo-photogrammetry is a well-established technique for 3D reconstruction of points in a scene (Luhmann et al., 2014). To estimate the 3D position of a point in a scene, it is necessary to know (i) the image coordinates of the point of interest in each image and (ii) the relative positions and orientations of the two cameras and details of their internal geometry (i.e. focal lengths, principal points, lens distortion coefficients). The first of these two steps is achieved through the process of image matching, and the second through camera calibration. When large numbers of corresponding points are matched between a pair of images, a disparity map is generated from which it is possible to use triangulation to generate high-resolution reconstructions of the surfaces of objects in a scene.

Stereo-photogrammetry reconstructions (hereafter referred to simply as 'stereo reconstructions') of the dorsal and ventral surfaces of the bird were generated independently using each camera pair (i.e. two dorsal, two ventral). The reconstructions from these four views were then aligned to form the complete bird. Reduced measurement quality near the edges of each reconstruction meant that these areas were removed, and an alternative approach was used to reconstruct the edge. Finally, the aligned stereo reconstructions and the edge reconstruction were transformed to a coordinate system amenable to flight mechanics analysis. Each part of this process is described in more detail below.

Disparity estimation—To maximise regions of the bird's surface visible to both cameras, a relatively low baseline-to-object distance ratio (~0.1) was used for each camera pair. This was beneficial for maximising the surface coverage of each stereo reconstruction, but could potentially reduce accuracy because the triangulation process used becomes more sensitive to matching errors. To maximise spatial density and matching accuracy, a recently developed area-based matching algorithm, 'Phase-correlation based Image Analysis System' (PCIAS) was used (Liu et al., 2012; Yan et al., 2012). PCIAS computes pixel-to-pixel disparity maps for image pairs using a scanning window that iteratively reduces in size, giving an increasingly refined estimate of the disparity map. The algorithm calculates the best match for a given window of pixels based on the phase correlation matrix of the Fourier transform of the two images (Morgan et al., 2010). This matching approach was specifically designed for very narrow baseline stereo-photogrammetry and has been demonstrated to outperform

commonly used matching algorithms such as normalised cross-correlation, achieving matching accuracies up to 1/50th pixel (Wu et al., 2012).

One limitation of area-based matching algorithms is a reduction in accuracy near the edges of objects in the scene with significant depth discontinuity. This was the case for the bird and the background, with parallax resulting in very different image information behind the bird in each image. This challenge was partially overcome by manually masking the background, with the mask offset by a half-window size outside the edge of the bird. However, the parallax still caused unrealistic edge artefacts in the 3D reconstructions. These errors were typically observed up to around a half-window size inside the edge of the bird, so the reconstructions of these pixels were not used. A window size of 32×32 pixels was used for all reconstructions except the dorsal surfaces of the peregrine falcon for flights P2 and P3 where a 16×16 window size generated slightly more accurate disparity maps. A median shift propagation filter size of 15×15 pixels was used to smooth the full-resolution disparity map.

3D reconstruction—Each camera pair was calibrated using the MATLAB computer vision system toolbox (2015a, The MathWorks Inc., Natick, MA, USA) based on images of the rigid board with an array of circular reference points. During the calibration process the extrinsic parameters (the relative positions and orientations of the cameras), the intrinsic parameters (the focal lengths and optical centres) and lens distortion coefficients were estimated based on fitting a model with these parameters to the image coordinates of the reference points in the calibration images (Zhang, 2000). Only the first two radial lens distortion coefficients were fitted, as testing showed negligible difference in taking additional distortion coefficients into account. Images with a high mean reprojection error (MRE>1 pixel) were removed, resulting in a MRE for all the stereo calibrations of less than 0.7 pixels. The image coordinates of the grid points were calculated semi-automatically using Calibration Toolbox v1.3.2 (Walker et al., 2009), and then used with MATLAB's 'estimateStereoParameters' function to compute the calibration. The images were undistorted prior to estimating the disparity map using PCIAS. The surface reconstructions were then generated using the MATLAB 'triangulate' function for each camera pair's disparity map and calibration.

Point cloud alignment—An additional calibration was conducted to calculate the relative positions and orientations of a single camera from each of the stereo pairs so that the surface reconstructions from each of the pairs could be aligned together. This was done using EasyWand5, a camera calibration algorithm utilising sparse bundle adjustment (Theriault et al., 2014) based on the images of the custom-made wand. The use of an additional calibration object was necessary as the spheres on the wand could be viewed by all cameras simultaneously, unlike the pattern on the rigid board. This calibration is referred to here as the 'global calibration'. The image coordinates of the wand spheres, as recorded by cameras 1, 3, 5 and 7, were estimated manually by drawing an ellipse around each sphere. The MRE across all cameras was 0.33 pixels for the global calibration.

Fixed-scale Helmert transformations were calculated between the 3D wand locations measured by each camera pair and those measured by the global calibration to obtain four

spatial similarity transformations used to align the stereo reconstructions in the coordinate system of the global calibration. The alignment was effective for stationary objects for which camera mis-synchronisation had negligible impact. For the flying birds, however, the camera mis-synchronisation (<1 ms) resulted in alignment errors that were resolved by applying iterative closest point alignment to the overlapping flight and tail feather regions of the point clouds using CloudCompare v2.8.1. Importantly, although the mis-synchronisation may have affected the alignment between the different surfaces, the shape of the bird was unlikely to have changed significantly over the <1 ms between images.

Edge reconstruction—A shape-carving approach adapted from Walker et al. (2012) was used to estimate the 3D outline (i.e. edge) of the bird. Shape carving works by retaining 3D points in the measurement volume that reproject onto silhouette images of the object of interest. To obtain the 3D outline, erosion and dilation were applied to silhouettes of the bird, leaving only the edge of the bird in each image. The shape-carving process then retained only points in the measurement volume that reprojected onto these ‘edge’ silhouettes, resulting in an approximately dorsoventral outline of the bird that followed the leading and trailing edges of the wings.

It was found that using all the globally calibrated cameras for the shape-carving process resulted in an accurate but sparse and unevenly distributed set of points. To increase the sampling density, multiple carving operations were carried out using all possible two-camera combinations from the global calibration. This significantly increased the number of points around the edge of the bird, but also introduced a large number of spurious points. These were removed using a distance threshold of 2 mm relative to the stereo reconstruction, leaving a continuous band of points around the edge of the bird. Spline fitting was then used to recover the clean, closed-loop outline of the bird, referred to here as the ‘edge spline’ (Fig. S2).

Geometric evaluation—To quantify the geometry of the wing, the reconstructed points in the coordinate system of the global calibration were transformed into a ‘wing–body’ oriented coordinate system using the method described in Fig. 3. Smoothing splines were then used to estimate dorsal, ventral and mean camber splines of wing cross-sections taken every 2 mm along the span (Fig. 4). The smoothing parameter for each spline was optimised using a *k*-fold cross-validation approach based on Breaz (2004).

For some sections, linear and quadratic polynomials were used instead of splines because they provided more robust representations of the raw points, being less sensitive to localised regions of increased noise or reduction in data coverage (i.e. near the wing tips). See Fig. S3 for details of how splines and polynomials were used across the span. Whichever was used, careful visual checks were carried out for each section to ensure the most effective approach was used that most accurately represented the raw points.

Measurements of spanwise camber, geometric twist, dihedral and sweep were obtained using the splines and polynomials. For each section, the chord was defined as the straight line joining the end points of the mean camber spline. Camber heatmaps were then generated based on the perpendicular distance between the mean camber spline and the

chord line. To visualise sweep and dihedral, the mean camber spline was evaluated at the quarter-chord for each section. This set of points was then projected on the *y*–*z* plane (dihedral) or *x*–*y* plane (sweep).

Wing span, mean aerodynamic chord and planform area were calculated based on Pennycuick (1989) using the edge spline. This approach was equivalent to that conventionally used in aircraft, where the planform area of the 'wing box' is included in the wing area. The ground velocity of the bird was estimated using the field video camera with the error estimate based on a position error of ±1 video frame. All estimates of standard deviation (s.d.) for velocity and AoA measurements were based on the anemometer measurements of wind velocity over a 5 s period (n=20) centred on the time the images were captured. The mean wing angle of attack was defined as the angle between the mean chord line of both wings and the mean flow velocity vector. Angle of sideslip was calculated as the angle between the mean flow velocity vector and the *x*-axis of the wing–body coordinate system. The coefficient of lift (C_L) was calculated based on wing area and an air density of 1.16 kg m^{-3}. Roll attitude and tail twist were defined as positive when the right side of the bird moved down.

To quantify the geometry of the tail, a plane was fitted to the manually segmented points of the dorsal surface of the rectrices (tail feathers). Tail twist (degree of rotation about the *x*-axis) and AoA were based on the partial derivatives of this plane. Longitudinal dihedral was defined as the difference between the zero-lift AoA of the wing and the zero-lift AoA of the tail. As the tail was approximately a flat plane (Fig. S4), it was assumed to generate zero lift when at a zero AoA. The birds' wings, however, were positively cambered so would generate zero lift at some small negative AoA. To account for this effect, the longitudinal dihedral was corrected by +5 deg. This estimate was based on data for the arm wing of a steppe eagle (Carruthers et al., 2010), which has a similar degree of camber to that of the wings measured here and should represent an overestimate of the effect of camber as the entire wing was not cambered.

Accuracy assessment—A rigid fibreglass model gull of similar size, shape and texture to a living bird was laser scanned to high accuracy (Romer Absolute Arm, RA-7525-SI, accuracy 0.063 mm) and used to assess the accuracy of the method based on images taken during field testing using the same camera setup and calibration data as used for the owl and peregrine falcon. The surface reconstructions and geometry measurements were made using the same methods as described above, except that point cloud alignment was done between the two dorsal surfaces and then between the two ventral surfaces, before using the global calibration to align the dorsal and ventral surfaces together. The dorsal–ventral alignment step based on aligning the flight feathers, as used with the live birds, was not required as mis-synchronisation was not an issue for the stationary model. For the live birds, mis-synchronisation (<1 ms) would have resulted in (i) error due to mis-synchronisation between the two cameras in each pair and (ii) error due to mis-synchronisation between pairs. The combined effect of these errors was a constant mis-alignment of the stereo reconstructions of the order ~10 mm that did not occur for the gull model. This mis-alignment was rectified for the live birds by iterative closest point alignment of the flight feathers and rectrices.

Results

Accuracy assessment

The distance between the points measured using the method presented here and the laser scan of the gull model was −0.016± 1.31 mm (mean±s.d. n=248,500). This was based on individually aligned reconstructions without the edges removed as this was most comparable to the other methods used previously (see Discussion). Fig. 5A shows the distribution of the error in the measurements for one dorsal camera pair and one ventral camera pair. There were localised regions of lower accuracy, particularly around the edges of the surface but also in some locations in the middle of the wing. These appeared to be due to errors in the disparity map which led to errors in the depth estimation. As can be seen in the cross-sections of the wing (Fig. 5B), these localised errors did not prevent the shape of the wing from being reconstructed relatively accurately. The spline reconstruction of the chordwise cross-sections showed very similar camber distributions for the laser and photogrammetric data (Fig. 5C, error −0.14±1.98 mm, n=248,500). The twist distribution measurement was relatively accurate for most of the wing (Fig. 5D, error 0.29±1.42 deg, n=497), but with regions of increased error near the wing roots and tips. The quarter-chord location was used to define the wing sweep (Fig. 5E, error −0.64±1.57 mm, n=497) and dihedral (Fig. 5F, error −0.02±0.90 mm, n=497) and had a very small error relative to the span and chord of the wing. The shape-carved outline for the model closely matched the laser scan outline (Fig. 5E) except in the region of the right shoulder and the tail. These regions were not visible because of the way the model was held, so the splining method interpolated across these gaps.

Flight conditions

The wind velocity showed significant temporal variation during the 5 s periods of flight measured (Table 1; Fig. S5), this is likely to have required the birds to make corrections to maintain a constant heading (Ravi et al., 2015). The video footage (Movies 1 and 2) showed that despite the variation in wind velocity, the trajectories of both birds were relatively smooth and direct. The barn owl flew with a consistent flap–glide–perch sequence and the three flights (O1–O3) were representative of all 10 flights conducted during fieldwork. Above the fence, the owl was banked slightly to the right in flight O1 and O2 and slightly to the left in O3. Flight O1 showed a roll to the left, flight O2 showed a fairly constant bank angle and flight O3 showed a roll to the right across the measurement volume. All the barn owl flights were completed with a perch manoeuvre onto the trainer’s glove, initiated just beyond the measurement volume.

The glide phase of the peregrine falcon flights (P1–P3) began earlier than for the barn owl, well before the fence, with a clear loss of altitude across the measurement volume. The peregrine falcon was banked slightly to the left prior to the fence during P1, after which the wings appeared to level out through the measurement volume. The wings appeared relatively level during P2 and P3, with the velocity and aft sweep clearly higher than during P1. During P3, the video footage showed a roll to the left immediately after the centre of the measurement volume, coinciding with the lowering of the left-wing tip.

Bird geometry and flight data

Fig. 6A shows examples of unprocessed point clouds (~1 point per mm^2 on average), with the edges removed for the dorsoventral, posteroanterior and lateral views of O1 and P1. Each individual point was assigned the RGB value of the corresponding pixel in the stereo reference image. The dorsoventral view also includes the edge spline and shows that removal of the edges did not result in a significant loss of surface coverage. In Fig. 6B, cross-sections taken every 10% span are shown for all flights, from the same camera view relative to the wing–body coordinate system, with distinct colours applied to the dorsal and ventral points. The aerofoil geometry changed markedly across the span, with increased thickness proximally towards the leading edge where the bones and muscles of the arm wing are located. The camber also appeared to reduce distally, where the sections are composed entirely of feathers. The edge spline is also plotted and shows that the tail is widely spread and twisted to the right in P1. Fig. 6B also shows that it was not possible to reconstruct the entire dorsal surface of the left wing in flights P2 and P3 because of the poor exposure in this region of the images. The dark coloration of the peregrine falcon's dorsal surface made it more challenging to reconstruct in these flights as a result of a reduction in natural light levels at the time.

Flight data derived from the reconstructed points, video footage and anemometer are provided in Table 1. The barn owl flights (O1–O3) showed generally similar configurations with negligible altitude change, suggesting that the bird was slowing down. Flights O1 and O3 were almost identical in wing planform (span, wing area, mean aerodynamic chord and aspect ratio). For flight O2, the span, area and air speed increased slightly, resulting in a lower required C_L for steady flight.

The peregrine falcon reduced its wing span, area and aspect ratio with increasing air speed and angle of attack, consistent with the findings for similar sized birds gliding in wind tunnels (Pennycuick, 1968; Rosen and Hedenstrom, 2001; Tucker, 1992; Tucker and Parrott, 1970). The glide angles and altitudes were very similar for all three configurations, showing that the bird was able to achieve consistent approach trajectories despite significant changes in flight conditions and configuration. The peregrine falcon had a significantly higher wing loading than the barn owl due mainly to its higher mass. This would have required it to fly at a higher velocity and/or C_L than the barn owl in order to generate sufficient lift.

Wing shape measurements

Both the peregrine falcon and the barn owl flights showed positively cambered wings, with higher camber in the arm region than in the hand (Fig. 7). Proximally, the magnitude and extent of the camber were greater in the peregrine falcon than in the barn owl and would contribute to the higher C_L calculated (Table 1). Subtle differences in the camber distribution between the flights were also visible. For example, the left wing of flight O1 showed slightly more camber distally than the right wing, while a similar but reversed asymmetry was visible in flight O3. The camber in flight O2 was also slightly larger distally than that of O3 and the right wing of O1. In the spanwise direction, the position of maximum camber, as measured from the leading edge of the wing, moved from approximately 75% chord proximally to 50% chord distally in all flights. The peregrine falcon showed rapid reduction

in camber at ±200 mm along the span, such that, distally, the camber was of similar magnitude to that of the barn owl. The camber reduced between flights P1 and P3, corresponding with the reduced C_L requirement between these flights (Table 1). A few localised regions showed small amounts of negative camber, mainly in the hand wing region.

Fig. 8 compares the spanwise AoA, sweep and dihedral for all flights. Because of the known spatial and temporal variation in flow velocity near the ground (Abdulrahim et al., 2010; Mohamed et al., 2014; Thompson et al., 2011; Watkins et al., 2006, 2010) and the distance of the anemometer from the centre of the measurement volume, the actual local AoA may have been slightly different to that shown. Fig. 8A is therefore a representation of spanwise angle of incidence referenced against the mean flow velocity. Both birds showed significant variation in twist along the span, with a marked change in gradient occurring in the vicinity of the wrist and manus. The barn owl adopted a relatively consistent morphology between flights (Fig. 8A,C), combining slight forward sweep with wash-out (pronation) proximally, and slight aft sweep with wash-in (supination) distally. Conversely, the peregrine falcon combined forward sweep with wash-in proximally and aft sweep with wash-out distally (Fig. 8A,C). Between P1 and P3, the magnitude of the proximal wash-in increased while the distal wash-out decreased. For all flights, the wings showed overall anhedral, though the barn owl featured some dihedral proximally (Fig. 8D).

Changes in configuration and asymmetries between the wings are also revealed in Fig. 8. The barn owl had twist asymmetry proximally in flights O1 and O3 and distally in O2. Between flights P1 and P3, the peregrine falcon swept its wings back, increased the anhedral and reduced the wash-out distally. The tail was also widely spread in P1, whereas in P2 and P3 it was furled. In P3, the right wing was 40 mm more extended than the left, equivalent to approximately 16% difference in area, and corresponded to a subtle asymmetry in sweep, where the left wrist was forward of the right. The video footage showed the peregrine falcon rolling to the left immediately after the centre of the measurement volume, suggesting that this asymmetry was for correctional control.

Discussion

Method performance

The method described in this paper represents a new combination of existing photogrammetric techniques, combining multi-view stereo-photogrammetry with a phase correlation-based image-matching algorithm to reconstruct the surfaces of free-flying birds. The accuracy of this method was compared with that of alternative approaches used previously where the accuracy of the method was reported (Table 2). Because of the different error estimation approaches used, comparisons should be made with care. Butz et al. (1985) measured the accuracy of their stereo-imaging by measuring the surface of a flat plate. The accuracy of the low-resolution arm wing profile measurements from a steppe eagle (Carruthers et al., 2010) was estimated using the strongly correlated linear relationship between MRE and 3D reconstruction error (Walker et al., 2009); however, no indication of the distribution of the error was reported. The 3D reconstruction accuracy from projected light measurements of a flapping barn owl wing was based on the assumption that the disparity error did not exceed 0.1 pixels (Wolf and Konrath, 2015). The visualisations of the

wing appeared to be of high accuracy, but no attempt was reported to quantify the error of the reconstructed points against an object of known shape. In contrast, the reconstruction error of a flapping pacific parrotlet was estimated using a sphere whose diameter was known to high accuracy (Deetjen et al., 2017). Comparison between the measured and nominal surface (similar to the approach presented here) enabled the mean and standard deviation of the error to be averaged over 400 frames. This approach was therefore of similar accuracy to the present results. Overall, the present method appears to have an accuracy comparable to that of other published methods, but because of the different methods of estimating accuracy, direct comparisons are difficult.

This method has the advantage of being able to be used with minimal physical infrastructure. It can be used outdoors or indoors provided there is sufficient light and can be used to image a relatively large volume with the cameras being a reasonable distance away from the flight line of the bird. This allows a high degree of flexibility in experimental setup, which may not be the case with approaches using projected light patterns. In this case, it allowed us to measure the gliding flight of the birds outdoors in natural conditions with unrestricted flight paths before and after the imaging volume.

The main novelty of this method is the use of computational image analysis for point matching based on the natural patterning of the birds. This allowed high-resolution disparity maps to be generated automatically. For the automated point matching to work, the stereo-images needed to be taken with a small baseline so the same points were visible in both images from a similar perspective. The use of phase-correlation then allowed a high-resolution disparity map to be generated. From the accuracy assessment made here, it would appear that errors in the disparity map were the main source of error in the shape of the reconstructed surfaces, with errors in the mapping creating localised regions with errors in depth manifesting as lumps. The accuracy of the surface reconstruction could be improved by zooming in the cameras so the image of the bird covered more of the optical sensor, reducing the magnitude of the errors in the disparity map relative to the physical dimensions of the bird. The trade-off would be a smaller imaging volume and the shorter shutter times required to prevent motion blur.

The main limitation of using an area-based point-matching algorithm was the need to remove poorly matched points around the wing edges due to background parallax. The use of shape carving improved the definition around the edges significantly, but future development of this method could focus on obtaining high-quality stereo reconstruction data close to the edges, potentially using feature-based matching approaches. An additional potential limitation is the need for sufficient natural patterning on the bird for point matching. However, this did not appear to be a major issue for the phase-correlation algorithm, as initial testing with a tawny eagle (*Aquila rapax*) with a relatively uniformly brown coloured dorsal surface performed well.

The method described here required manual masking of images and manual selection of alternative fitting methods for wing cross-sections in areas of reduced quality, such as near the wing tips. In the future, automated masking and fitting method selection could increase the automation of the process. In comparison, previous low-resolution methods (Table 2)

have involved time-intensive manual point matching, which was not required here, but was required by Wolf and Konrath (2015) for initialisation of the automated matching algorithm used. The advantage of the method of Deetjen et al. (2017) is that processing of each image did not require any manual input but did have the limitation of only reconstructing a single surface.

The accuracy analysis showed that the method presented had sufficient accuracy to measure a range of geometric features of interest. These features are useful for flight dynamics analysis as will be demonstrated for the case of the measured barn owl and peregrine falcon flights. However, the measured surfaces did have some localised regions with higher error, which meant that the wing surface was not smooth in places, when by eye the wing overall had a smooth surface. These regions appeared to be relatively localised, so smoothing could potentially recover the smooth wing surface. Previous studies of bird wing geometry based on laser scans of dead wings have found that fitting mathematical functions representing aerofoil parameters can effectively model the cross-sectional geometry of avian wings (Klän et al., 2009; Liu et al., 2006). This approach was also successfully used for smoothing photogrammetric reconstructions of a barn owl wing through its flapping cycle (Wolf and Konrath, 2015). Therefore, it would appear that function fitting or similar smoothing approaches could be used alongside the method presented here to reconstruct complete smooth wing cross-sections. These geometries could then be used for both experimental and computational aerodynamic analysis.

As presented here, this method allows the in-flight geometry of gliding birds of prey to be measured accurately, including wing camber, twist, sweep and dihedral. The utility of this novel method and the results it can produce are illustrated below in the context of assessing aspects of flight stability and control for the measured flights of the barn owl and peregrine falcon.

In-flight geometries

The barn owl flew relatively consistently in terms of speed, AoA and configuration for the three flights analysed (Table 1), with these flights being generally representative of all 10 flights carried out during data collection. Measurements of the wing showed positive camber that reduced in magnitude distally (Fig. 7), combined with significant spanwise wash-in, relatively little sweep and moderate anhedral (Fig. 8). In contrast, the peregrine falcon flights showed significant differences in flight speed, AoA (Table 1), wing twist, sweep, dihedral and tail configuration (Fig. 8). The only consistent geometric feature between the peregrine falcon flights was distally reduced camber (Fig. 7).

Static longitudinal stability

The measured glide geometries can be assessed in relation to the contributions of different geometric aspects to static longitudinal stability as introduced earlier. The barn owl had a positively cambered wing in the arm wing region, with the camber effectively reducing to zero distally (Fig. 7). This positive camber would generate a nose-down zero-lift pitching moment (Fig. 1D). The drag-based contribution to the zero-lift pitching moment was probably negligible because of the likely small magnitude of drag relative to lift and because

the moment arm would have been reduced by wing anhedral (Figs 6A and 8D). The barn owl combined a small amount of forward sweep with wash-out proximally, with a small amount of aft-sweep with wash-in distally (Fig. 8A,C). Neglecting camber, these features could contribute towards a negative zero-lift pitching moment (Fig. 1H). However, the distally reducing camber may have served to reduce the contribution of the sweep and twist to the zero-lift pitching moment, such that the overall contribution was likely to be negligible.

The mean angle of incidence of the wing was substantially less than the angle of incidence of the owl's tail in all flights (Table 1). Taking into consideration an estimated correction for the effects of wing camber, this still resulted in a high degree of longitudinal anhedral, which would contribute towards a negative zero-lift pitching moment (Fig. 1J). Although there is an approximation made in the correction for camber, this should be an overestimate which would make measurements of longitudinal anhedral more conservative. There is some uncertainty in the exact degree of longitudinal anhedral because of the potentially complex aerodynamic interaction of the wings and tail, but it has been shown that the presence of a bird's wings does not significantly change the lift generated by the tail for similar angles of attack and spread angles as measured here (Evans, 2003). Another aspect to consider is that if the owl were longitudinally statically stable it would require a large degree of longitudinal dihedral to counter the nose-down moment created by the positively cambered wing. This would mean the tail would need to be at a large negative angle of incidence relative to the wing (Fig. 1I) and this is clearly not the case. Overall, the positively cambered wing and the longitudinal anhedral seen in the barn owl would appear to be indicative of a negative zero-lift pitching moment, which given the observed trimmed flight, suggests it was longitudinally statically unstable in the flights measured.

The peregrine falcon's wings were more positively cambered than those of the barn owl (Fig. 7), implying an increased nose-down zero-lift pitching moment. Similar to the barn owl, any drag-based contribution to the zero-lift pitching moment in the peregrine falcon was probably negligible due to wing anhedral (Figs 6A and 8D). In contrast to the barn owl, the peregrine falcon combined forward sweep with wash-in proximally and aft-sweep with wash-out distally, which, combined with distally reduced camber, would generate a nose-up zero-lift pitching moment. For flight P1, the peregrine falcon showed longitudinal anhedral, but this was much smaller in P2 and P3 (Table 1). It is therefore unclear whether the combined contributions of wing camber, longitudinal anhedral and the combinations of sweep and twist would result in a nose-up or nose-down zero-lift pitching moment. This makes it difficult to assess whether the peregrine falcon was statically longitudinally stable or unstable in the flights measured. Further work is required to relate the measured geometries of both birds to their aerodynamic and inertial properties (i.e. centre of mass and mass moments of inertia) to enable further flight dynamics modelling to quantify the stability of the birds during these flights.

Flight control

Correctional control is required to maintain a desired flight path, whether a configuration is stable or unstable (Taylor, 2005). Temporal variation was measured in the wind flows during

all flights (Table 1; Fig. S5) and as such it is likely that the birds needed to compensate for these variations in order to maintain their flight path to their landing point. Geometric features such as wing asymmetry, which could contribute to flight control, were observed in flights of both the barn owl and peregrine falcon. The barn owl reconstructions revealed asymmetry in camber (Fig. 7), spanwise AoA (Fig. 8A) and tail twisting (Table 1). Between the fence and the centre of the measurement volume, flights O1 and O3 showed rolls to the left and right, respectively (Movies 1 and 2), corresponding to asymmetry in camber distally and AoA proximally, that may have been used to annul the roll rate (Warrick et al., 1998). The camber distribution was more symmetric for flight O2, though it was combined with asymmetric spanwise AoA that ought to have generated a roll to the right not observed in the video footage. During O1, upward deflections of the secondary flight feathers on the right wing were observed in the video footage that may correspond to the proximal twist asymmetry in Fig. 8A.

The peregrine falcon flights P1 and P2 were generally symmetric, while flight P3 showed asymmetry in span and sweep as a result of the partial retraction of the left wing (Fig. 8B). This corresponds to the video footage (Movies 1 and 2), which shows the bird rolling to the left immediately after the centre of the measurement volume. This was consistent with observations of birds using span asymmetry as a means of roll control (Dudley, 2002; Sachs, 2007; Warrick et al., 2002). The peregrine falcon showed significant variation in sweep, span, angle of attack, flight velocity and tail spread across the reconstructed flights (Table 1 and Fig. 8). This is generally consistent with observations of birds trained to glide steadily in tilting wind tunnels (Evans et al., 2002; Henningsson and Hedenstrom, 2011; Pennycuick, 1968; Rosen and Hedenstrom, 2001; Tucker, 1992; Tucker and Parrott, 1970). Birds actively modulate their wing area with AoA and flow velocity to control their lift to drag ratio. Aerodynamic force measurements on the wings of dead peregrine falcons showed that the lift to drag ratio was insensitive to changes in sweep angle at a given AoA, and may allow the bird to modulate its velocity and wing area without affecting glide angle (Klaassen van Oorschot et al., 2016). The present results reveal that the glide angle of the peregrine falcon varied by less than 0.5 deg between flights, despite significant changes in air speed, AoA, camber, wing sweep, anhedral, tail spread and tail AoA (Table 1). This suggests that a range of geometric configurations may be able to generate consistent glide performance.

Concluding remarks

The novel method presented here represents a new combination of existing photogrammetric techniques, combining multi-view stereo-photogrammetry with a phase correlation-based image-matching algorithm to obtain accurate measurements of the surface geometries of flying birds. The main novelty of this method is the use of computational image analysis for point matching based on the natural patterning of the birds. The advantages of this method are that it can be used outdoors or indoors with minimal infrastructure and can be used to image a relatively large volume while being non-intrusive for the birds. The main limitations of the method are that it cannot accurately reconstruct the very edges of the wings and that the surface can show local regions of lower accuracy when errors occur in the image - matching algorithm. However, the accuracy assessment showed that the method is sufficiently accurate to enable measurement of the geometric parameters considered here.

Europe PMC Funders Author Manuscripts

The utility of the method was shown by measuring the geometry of a barn owl and a peregrine falcon at a single instant in time, during three gliding flights per bird. The barn owl flew with a consistent geometry and the positive wing camber and longitudinal anhedral seen were indicative of a negative zero-lift pitching moment, which suggests it was longitudinally statically unstable in the flights measured. The peregrine falcon flew at a range of airspeeds, but with a consistent glide path angle. Related to the different airspeeds, the bird flew with a range of geometric parameters which made it difficult to assess whether the peregrine falcon was statically longitudinally stable or unstable in the flights measured. Aspects in the geometries adopted by both birds appeared to be related to control corrections and this method would be well suited for future investigations in this area under more aerodynamically controlled conditions. Overall, this method for reconstructing the geometry of freely flying birds has the potential to enable a range of new quantitative studies of avian flight dynamics and control.

Supplementary Material

Refer to Web version on PubMed Central for supplementary material.

Acknowledgements

We would like to thank bird trainers Lloyd and Rose Buck (http://www.lloydbuck.co.uk/), Patrick Metcalfe (University of Bristol) for assistance in the fieldwork, Dayton Taylor (Digital Air, Geneva, http://www.digitalair.com/) for providing the camera synchronisation equipment, Ty Hedrick (University of North Carolina at Chapel Hill) for the use of EasyWand5, Simon Walker (University of Oxford) for use of Calibration Toolbox v1.3.2 and shape-carving code, Andrew Hughes for use of Fenswood Farm where the experiment took place and the staff of the University of Bristol Faculty of Engineering workshop who manufactured various items of equipment. Thanks also to Jorn Cheney (Royal Veterinary College) and Jonathan Stevenson (University of Bristol) for their guidance and advice during preparation of the manuscript.

Funding

This project has received funding from the European Research Council (ERC) under the European Union's Horizon 2020 research and innovation programme (grant agreement no. 679355 to S.P.W.); and a Doctoral Training Grant (to N.E.D.) from the Engineering and Physical Sciences Research Council (EPSRC).

References

Abdulrahim M, Watkins S, Segal R, Marino M, Sheridan J. Dynamic sensitivity to atmospheric turbulence of unmanned air vehicles with varying configuration. J Aircraft. 2010; 47:1873–1883. DOI: 10.2514/1.46860

Anderson, JD. Aircraft Performance and Design. Singapore: McGraw-Hill; 1999.

Anderson, JD. Fundamentals of Aerodynamics. New York: McGraw-Hill; 2007.

Biesel, W, Butz, H, Nachtigall, W. Erste messungen der flugelgeometrie bei frei gleitfliegenden haustauben (*Col. liv. var. dom.*) unter benutzung neu ausgearbeiteter verfahren der windkanaltechnik und der stereophotogrammetrieBiona Report 3: Bird Flight - Vogelflug. Nachtigall, W, editor. Saarbrücken: Gustav Fischer Verlag; 1985. 139–160.

Bilo D. Flugbiophysik von kleinvogeln I. Kinematik und aerodynamik des flugelabschlages beim haussperling (*Passer domesticus l.*). Z Vergl Physiol. 1971; 71:382–454. DOI: 10.1007/BF00302374

Bilo D. Flugbiophysik von kleinvogeln II. Kinematik und aerodynamik des flugelaufschlages beim haussperling (*Passer domesticus l.*). Z Vergl Physiol. 1972; 76:426–437. DOI: 10.1007/BF00337783

Bilo, D, Nachtigall, W. Movements of a sparrow's wings during free flight in a wind tunnel, demonstrated by stereoscopic anaglyphic prints from high speed rotating-disc camera

photographsBiona Report 3: Bird Flight - Vogelflug. Nachtigall, WN, editor. Saarbrücken: Gustav Fischer Verlag; 1985. 161–169.

Breaz N. The cross-validation method in smoothing spline regression. Acta Universitatis Apulensis. 2004; 7:77–84.

Brill C, Mayer-Kunz DP, Nachtigall W. Wing profile data of a free-gliding bird. Naturwissenschaften. 1989; 76:39–40. DOI: 10.1007/BF00368314

Butz, H, Biesel, W, Nachtigall, W. Einsatz spezieller methoden der photogrammetrie zur untersuchung der flugelgeometrie frei gleitfliegender taubenBiona Report 3: Bird Flight - Vogelflug. Nachtigall, W, editor. Saarbrücken: Gustav Fischer Verlag; 1985. 123–138.

Carruthers AC, Walker SM, Thomas ALR, Taylor GK. Aerodynamics of aerofoil sections measured on a free-flying bird. Proc IMechE Part G J Aero Eng. 2010; 224:855–864. DOI: 10.1243/09544100JAERO737

Cook, MV. Flight Dynamics Principles. Oxford: Butterworth-Heinemann; 1997.

Deetjen MR, Biewener AA, Lentink D. High-speed surface reconstruction of a flying bird using structured light. J Exp Biol. 2017; 220:1956–1961. DOI: 10.1242/jeb.149708 [PubMed: 28348041]

Dudley R. Mechanisms and implications of animal flight maneuverability. Integr Comp Biol. 2002; 42:135–140. DOI: 10.1093/icb/42.1.135 [PubMed: 21708702]

Durston NE, Wan X, Liu JG, Windsor SP. Data from: Avian surface reconstruction in free-flight with application to flight stability analysis of a barn owl and peregrine falcon. Dryad Digital Repository. 2019; doi: 10.5061/dryad.sf755pr

Etkin, B, Reid, D. Dynamics of Flight - Stability and Control. New York: John Wiley and Sons, Inc.; 1996.

Evans MR. Birds' tails do act like delta wings but delta-wing theory does not always predict the forces they generate. Proc R Soc B Biol Sci. 2003; 270:1379–1385. DOI: 10.1098/rspb.2003.2373

Evans MR, Rosén M, Park KJ, Hedenström A. How do birds' tails work? Delta-wing theory fails to predict tail shape during flight. Proc R Soc B Biol Sci. 2002; 269:1053–1057. DOI: 10.1098/rspb.2001.1901

Henningsson P, Hedenstrom A. Aerodynamics of gliding flight in common swifts. J Exp Biol. 2011; 214:382–393. DOI: 10.1242/jeb.050609 [PubMed: 21228197]

Klaassen van Oorschot B, Mistick EA, Tobalske BW. Aerodynamic consequences of wing morphing during emulated take-off and gliding in birds. J Exp Biol. 2016; 219:3146–3154. DOI: 10.1242/jeb.136721 [PubMed: 27473437]

Klän S, Bachmann T, Klaas M, Wagner H, Schröder W. Experimental analysis of the flow field over a novel owl based airfoil. Exp Fluids. 2009; 46:975–989. DOI: 10.1007/s00348-008-0600-7

Liu T, Kuykendoll K, Rhew R, Jones S. Avian wing geometry and kinematics. AIAA J. 2006; 44:954–963. DOI: 10.2514/1.16224

Liu JG, Yan H, Morgan G. PCIAS subpixel technology. Meas Control. 2012; 45:207–211. DOI: 10.1177/002029401204500702

Luhmann, T, Robson, S, Kyle, S, Boehm, J. Close-range Photogrammetry and 3D Imaging. Berlin: Walter de Gruyter; 2014.

Maeda M, Nakata T, Kitamura I, Tanaka H, Liu H. Quantifying the dynamic wing morphing of hovering hummingbird. R Soc Open Sci. 2017; 4doi: 10.1098/rsos.170307

Mohamed A, Massey K, Watkins S, Clothier R. The attitude control of fixed-wing MAVS in turbulent environments. Prog Aerosp Sci. 2014; 66:37–48. DOI: 10.1016/j.paerosci.2013.12.003

Morgan GLK, Liu JG, Yan H. Precise subpixel disparity measurement from very narrow baseline stereo. IEEE T Geosci Remote. 2010; 48:3424–3433. DOI: 10.1109/TGRS.2010.2046672

Nickel, K, Wohlfahrt, M. Tailless Aircraft in Theory and Practice. Washington DC: AIAA; 1994.

Pennycuick CJ. A wind tunnel study of the gliding flight in the pigeon, *Columba Livia*. J Exp Biol. 1968; 49:509–526.

Pennycuick, CJ. Bird Flight Performance: A Practical Calculation Manual. New York: Oxford University Press; 1989.

Ravi S, Crall JD, McNeilly L, Gagliardi SF, Biewener AA, Combes SA. Hummingbird flight stability and control in freestream turbulent winds. J Exp Biol. 2015; 218:1444.doi: 10.1242/jeb.114553 [PubMed: 25767146]

Rosen M, Hedenstrom A. Gliding flight in a Jackdaw: a wind tunnel study. J Exp Biol. 2001; 204:1153–1166. [PubMed: 11222131]

Sachs G. Why birds and miniscale airplanes need no vertical tail. J Aircraft. 2007; 44:1159–1167. DOI: 10.2514/1.20175

Taylor GK. Flight muscles and flight dynamics: towards an integrative framework. Anim Biol. 2005; 55:81–99. DOI: 10.1163/1570756053276871

Theriault DH, Fuller NW, Jackson BE, Bluhm E, Evangelista D, Wu Z, Betke M, Hedrick TL. A protocol and calibration method for accurate multi-camera field videography. J Exp Biol. 2014; 217:1843–1848. DOI: 10.1242/jeb.100529 [PubMed: 24577444]

Thomas ALR, Taylor GK. Animal flight dynamics I. Stability in gliding flight. J Theor Biol. 2001; 212:399–424. DOI: 10.1006/jtbi.2001.2387 [PubMed: 11829360]

Thompson M, Watkins S, White C, Holmes J. Span-wise wind fluctuations in open terrain as applicable to small flying craft. Aeronaut J. 2011; 115:693–701. DOI: 10.1017/S0001924000006412

Tobalske BW. Biomechanics of bird flight. J Exp Biol. 2007; 210:3135.doi: 10.1242/jeb.000273 [PubMed: 17766290]

Tucker VA. Pitching equilibrium, wing span and tail span in a gliding harris' hawk, *Parabuteo uncinctus*. J Exp Biol. 1992; 165:21–41.

Tucker VA, Parrott GC. Aerodynamics of gliding flight in a falcon and other birds. J Exp Biol. 1970; 52:345–367.

Walker SM, Thomas ALR, Taylor GK. Photogrammetric reconstruction of high-resolution surface topographies and deformable wing kinematics of tethered locusts and free-flying hoverflies. J R Soc Interface. 2009; 6:351–366. DOI: 10.1098/rsif.2008.0245 [PubMed: 18682361]

Walker SM, Thomas ALR, Taylor GK. Operation of the alula as an indicator of gear change in hoverflies. J R Soc Interface. 2012; 9:1194–1207. DOI: 10.1098/rsif.2011.0617 [PubMed: 22072452]

Warrick RW, Dial KP, Biewener AA. Asymmetrical force production in the maneuvering flight of pigeons. The Auk. 1998; 115:916–928. DOI: 10.2307/4089510

Warrick DR, Bundle MW, Dial KP. Bird maneuvering flight: blurred bodies, clear heads. Integr Comp Biol. 2002; 42:141–148. DOI: 10.1093/icb/42.1.141 [PubMed: 21708703]

Watkins S, Milbank J, Loxton BJ, Melbourne WH. Atmospheric winds and their implications for microair vehicles. AIAA J. 2006; 44:2591–2600. DOI: 10.2514/1.22670

Watkins S, Thompson M, Loxton B, Abdulrahim M. On low altitude flight through the atmospheric boundary layer. Int J Micro Air Veh. 2010; 2:55–68. DOI: 10.1260/1756-8293.2.2.55

Withers PC. The aerodynamic performance of the wing in red-shouldered hawk *Buteo linearis* and a possible aeroelastic role for wing-tip slots. Ibis. 1981; 123:239–247. DOI: 10.1111/j.1474-919X.1981.tb00933.x

Wolf T, Konrath R. Avian wing geometry and kinematics of a free-flying barn owl in flapping flight. Exp Fluids. 2015; 56:28.doi: 10.1007/s00348-015-1898-6

Wu, M-C; Liu, JG; Yan, H; Mason, PJ. Three-dimensional surface displacement map of the 2008 Wenchuan earthquake derived from phase correlation (PC) sub-pixel offset method and adaptive local kriging (ALK) DInSAR data. IEEE International Geoscience and Remote Sensing Symposium; Munich, Germany. IEEE; 2012.

Yan, H; Liu, J-G; Morgan, G; Liu, C-C. High quality DEM generation from PCIAS. IEEE Int Geosci Remote Se; Munich, Germany. IEEE; 2012.

Zhang Z. A flexible new technique for camera calibration. IEEE Trans Pattern Anal Machine Intell. 2000; 22:1330–1334. DOI: 10.1109/34.888718

Europe PMC Funders Author Manuscripts

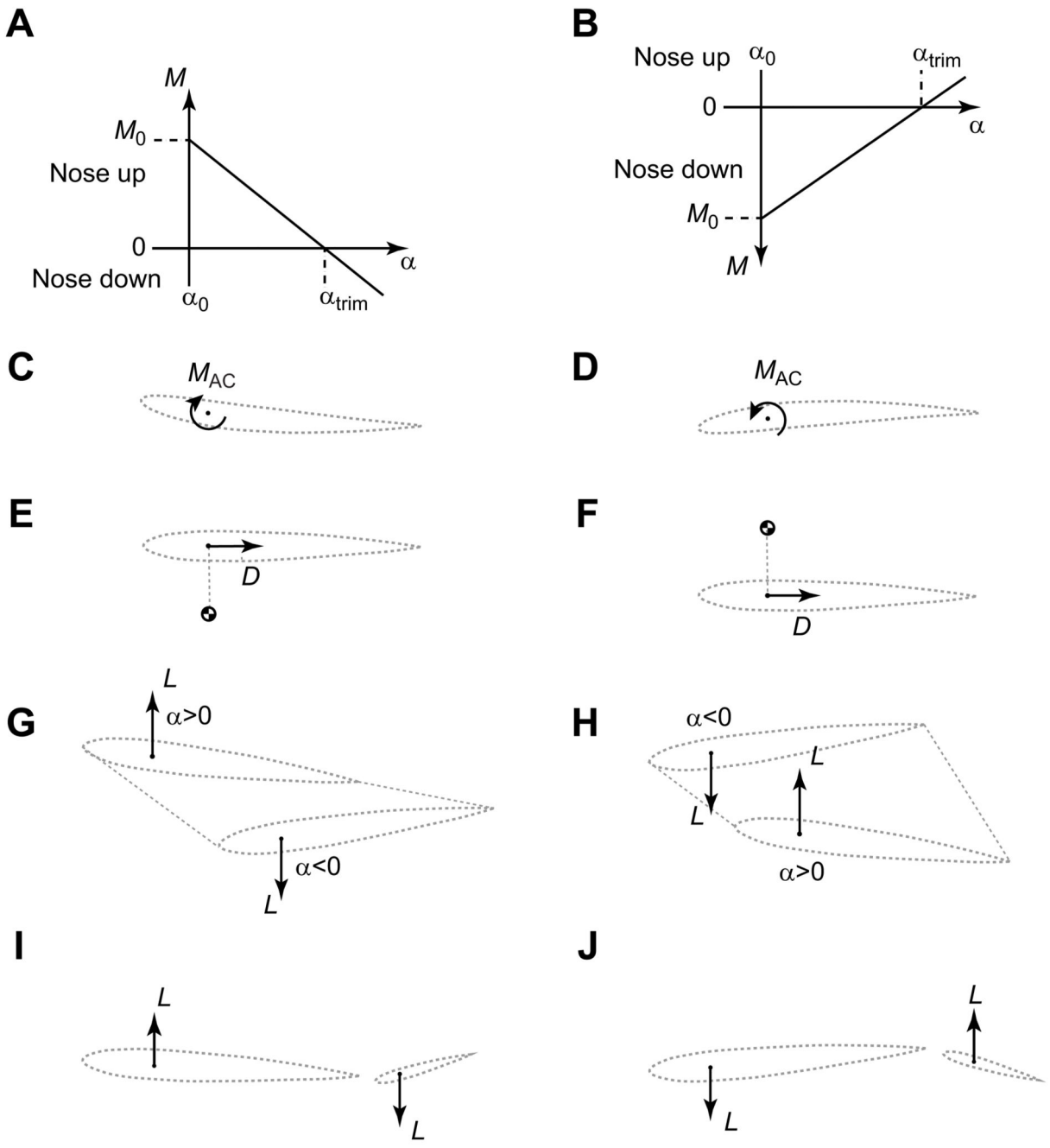

Fig. 1. Geometric indicators of longitudinal static stability based on their contribution to zero-lift pitching moment.

The relationship between pitching moment and angle of attack (AoA) for stable (A) and unstable (B) configurations. Assuming a linear moment slope, to trim a stable configuration requires a positive (nose-up) zero-lift pitching moment (C,E,G,I), while unstable configurations require a negative (nose-down) zero-lift pitching moment (D,F,H,J). Wing camber (C,D), vertical wing position relative to centre of mass (E,F), combinations of wing sweep and twist (G,H) and longitudinal dihedral/anhedral (I,J) can all generate both positive and negative zero-lift pitching moments depending on their configuration. Each

configuration is shown for zero total lift. Drag is not shown where its contribution is negligible. α, AoA; α_0, zero-lift AoA; α_{trim}, AoA at which forces and moments sum to zero; M, pitching moment; M_0, zero-lift pitching moment; M_{AC}, pitching moment of cambered aerofoil about its aerodynamic centre; D, drag; L, lift.

Europe PMC Funders Author Manuscripts

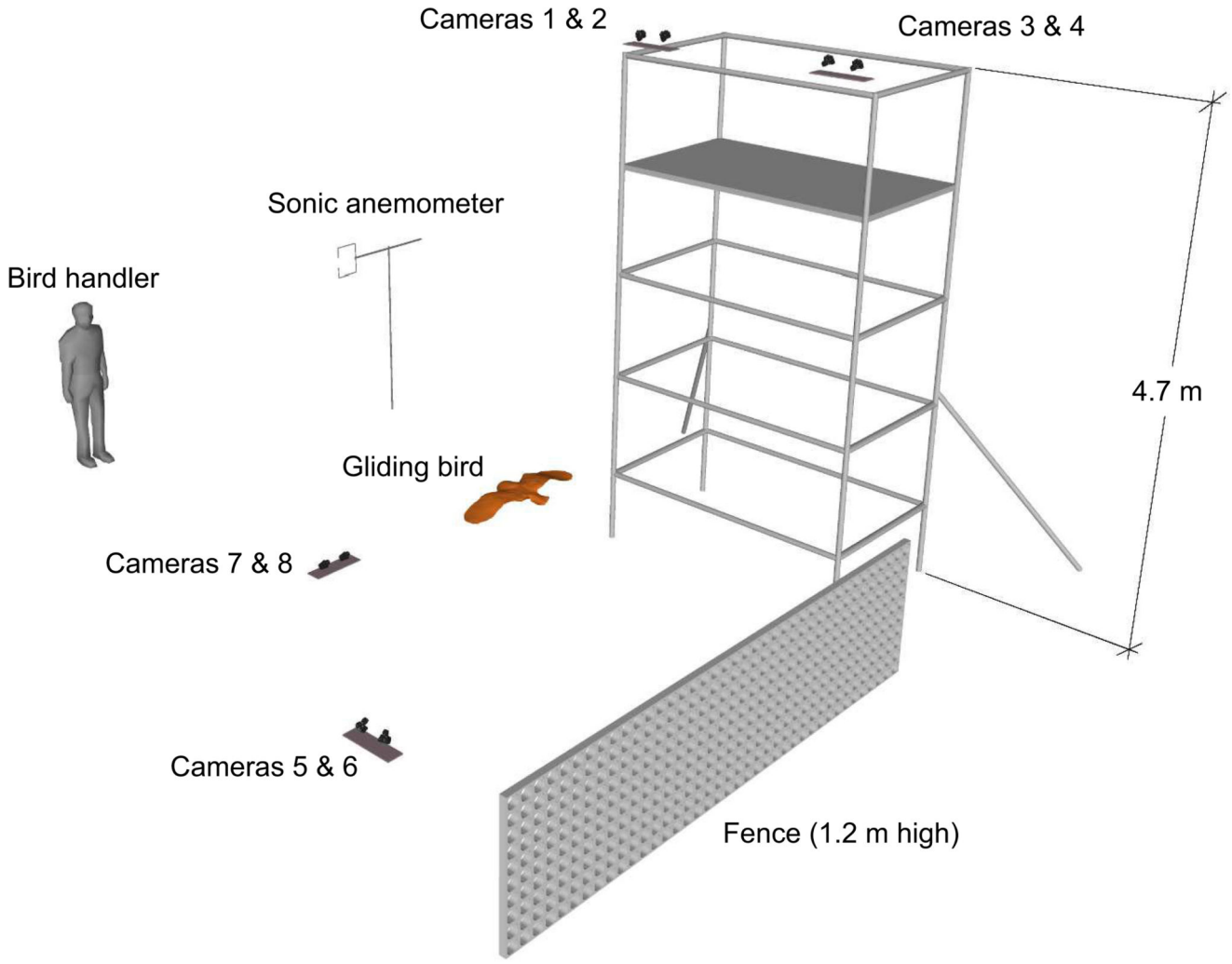

Fig. 2. Scale view of experimental setup.

Cameras 1–4 were mounted on a mobile access tower, while cameras 5–8 were mounted on custom-made supports recessed into the ground to maximise the field of view. Example images from each pair are shown in Fig. S1.

Europe PMC Funders Author Manuscripts

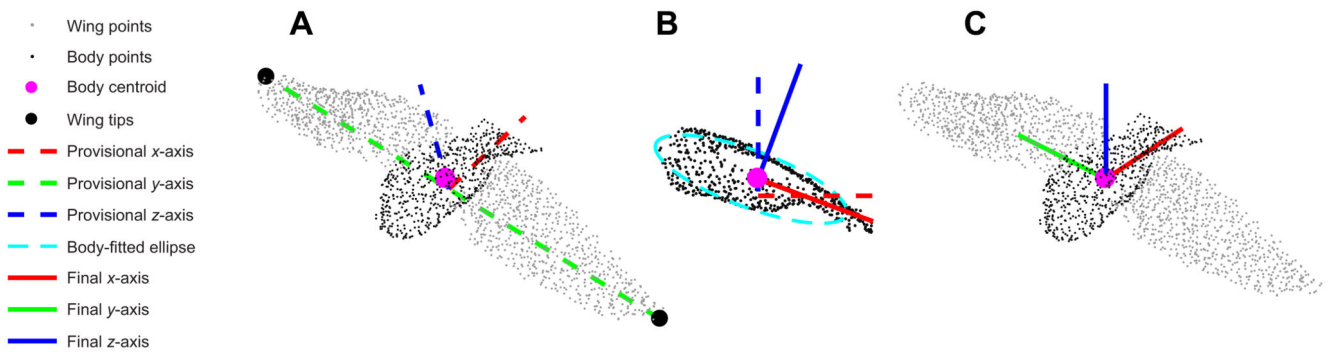

Fig. 3. Fitting a coordinate system to the wings and body of the bird.

(A) Evenly resampled points in the global coordinate system were segmented manually into body and wings. The wing and body points have been further resampled in the figure for clarity. The origin was calculated using the centroid of the body and tail, with the two points on each wing furthest from the origin defining a provisional *y*-axis. A provisional *z*-axis was then calculated as the line coincident with the origin and perpendicular to the provisional *y*-axis. The cross-product of the provisional *y*- and *z*-axes resulted in the provisional *x*-axis. (B) The final anteroposterior (*x*) and ventrodorsal (*z*) axes were defined, respectively, by the major and minor axes of an ellipse fitted to the body and tail data projected onto the sagittal plane defined by the provisional *x*- and *z*-axes. (C) The final wing–body fitted coordinate system in which the final *y*-axis is parallel to the provisional *y*-axis and is coincident with the origin.

Europe PMC Funders Author Manuscripts

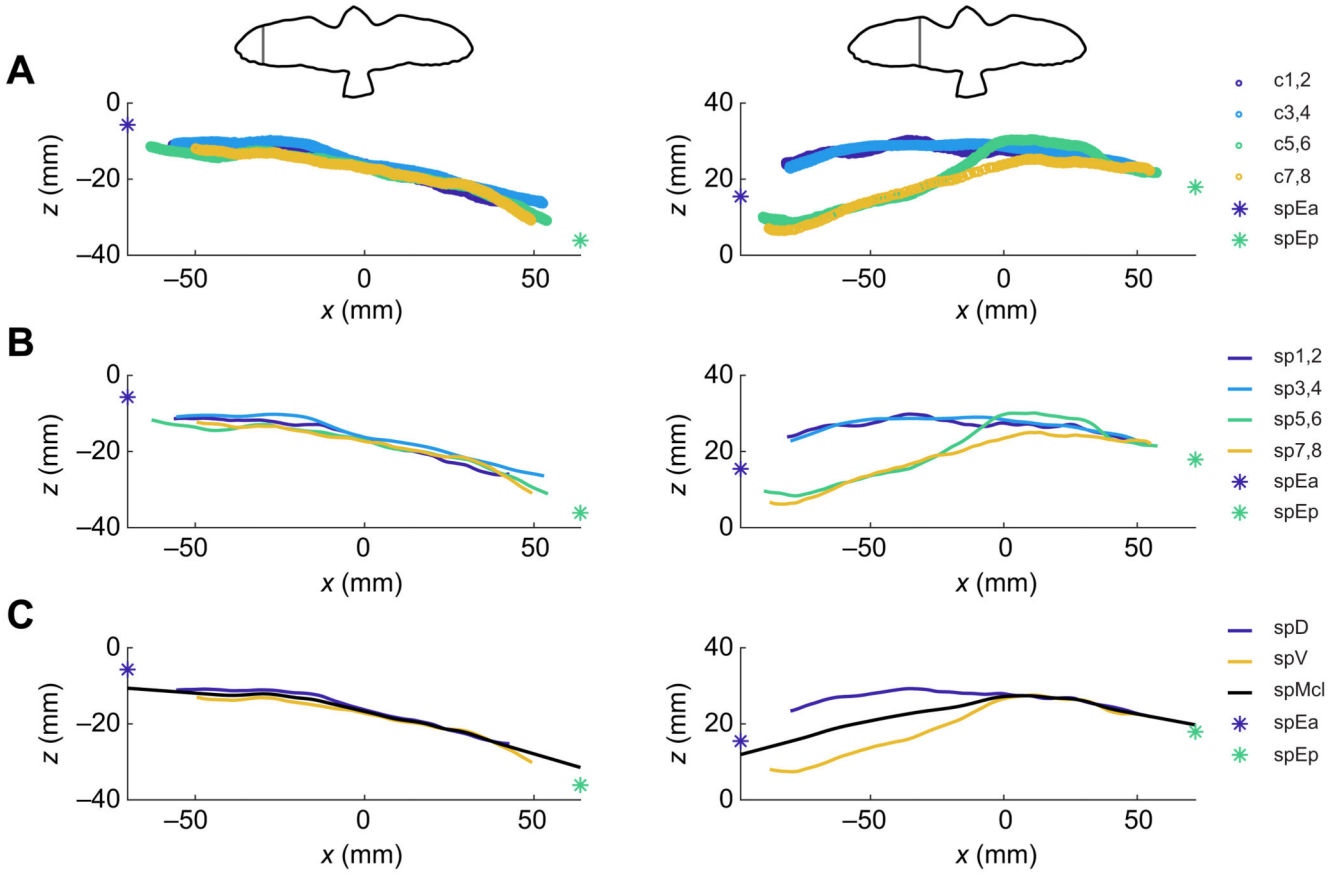

Fig. 4. Generation of the dorsal, ventral and mean camber splines.

This is illustrated using representative sections from the arm wing (left) and hand wing (right) of flight O1. The *z*-axis is slightly stretched for clarity. The edge spline anterior and posterior positions (spEa, spEp) are shown in each plot. (A) The raw data from each stereo camera pair (upper surface: c1,2, c3,4; and lower surface: c5,6, c7,8) for the section. (B) Smoothing spline fits to each dataset (sp1,2, sp3,4, sp5,6 and sp7,8). (C) The resulting dorsal (spD), ventral (spV) and mean camber line splines (spMcl) used to measure camber, twist, sweep and dihedral based on averaging the splines generated in B. The mean camber spline required extrapolation to the *x*-coordinates of the anterior and posterior edge spline data points, spEa and spEp.

Europe PMC Funders Author Manuscripts

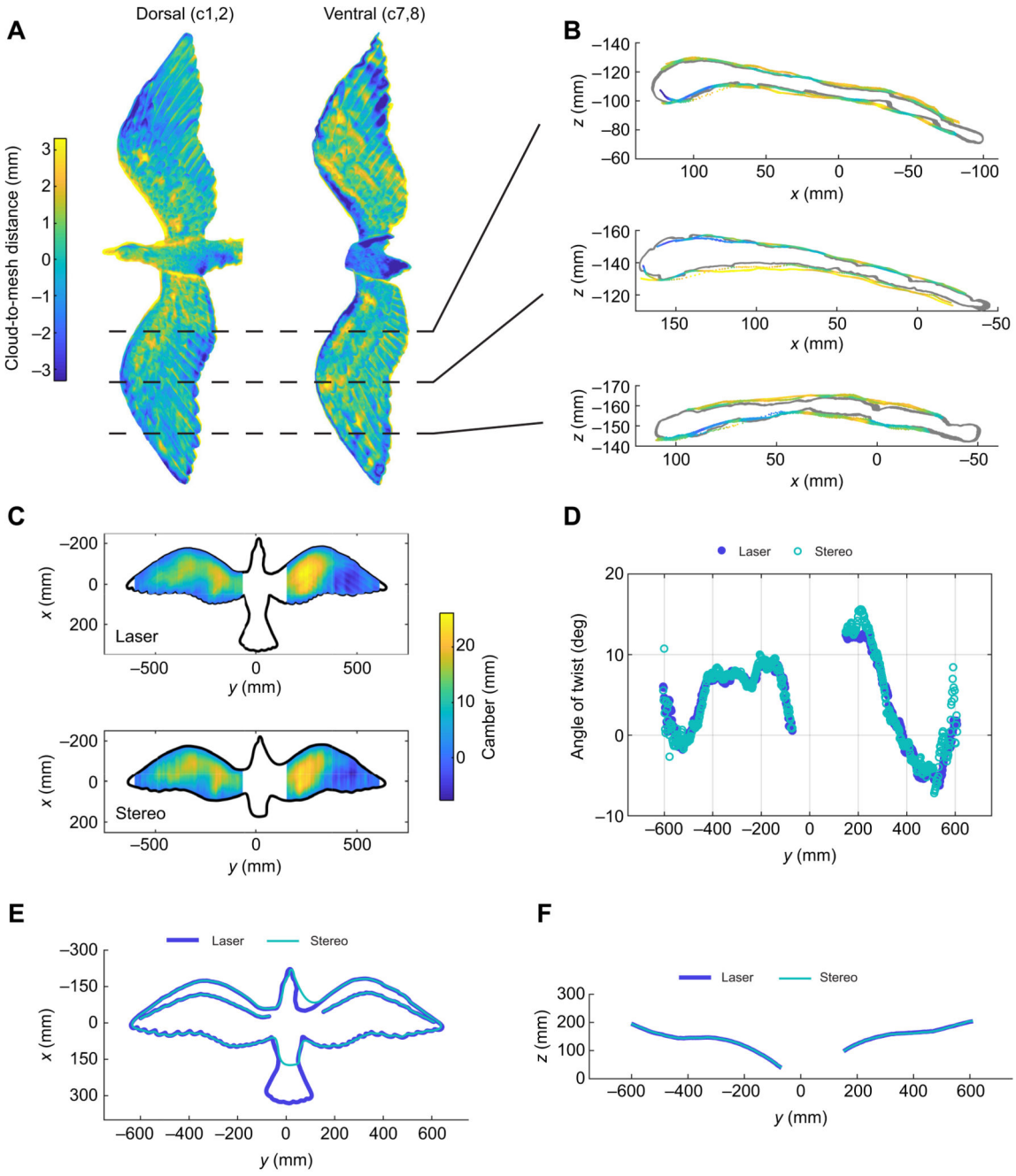

Fig. 5. Assessment of the accuracy of the stereo reconstructions by comparison with a high-accuracy laser scan of a fibreglass gull model.

(A) Planform views of the errors for stereo reconstructions (edges retained) individually aligned to the laser scan. (B) Cross-sections through the wing showing the difference between the laser scan (grey points) and the reconstructed points based on collective alignment to the laser scan. The points are coloured by their error value using the same colour scale as in A. (C) Scalar fields quantifying distance between the mean camber line and chord line, as measured perpendicular to the chord line, for sections every 2 mm along the span for the laser scan and the stereo-photogrammetry reconstruction. (D) Spanwise

twist distributions for both datasets. (E) Dorsoventral view of both datasets showing the quarter-chord wing sweep and the planform outline. (F) Posteroanterior view of the quarter-chord of both datasets, showing the wing dihedral.

Europe PMC Funders Author Manuscripts

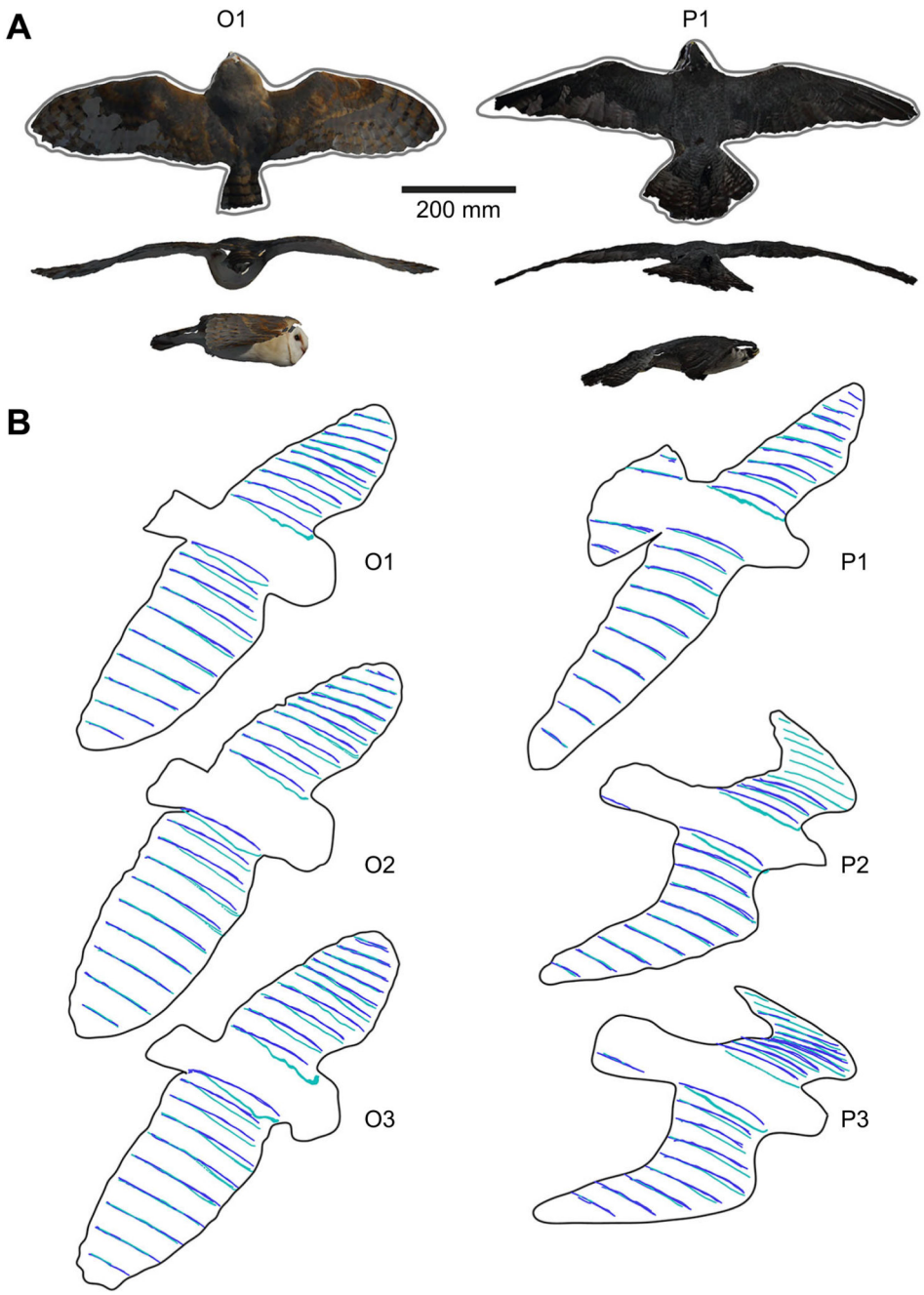

Fig. 6. Overview of reconstructed geometry.

(A) Point clouds with edges removed for flights O1 and P1 in wing–body coordinates, showing (top to bottom) dorsoventral, posteroanterior and lateral views, with the points coloured by the RGB pixel values from the reference image. The edge spline is shown in the dorsoventral view. (B) Spline fitted wing sections every 10% span for all flights including the edge spline. See Fig. S6 for a comparison of the wing section raw and spline fitted data and Movie 3 for a 3D view of the raw data for flights O1 and P1.

Europe PMC Funders Author Manuscripts

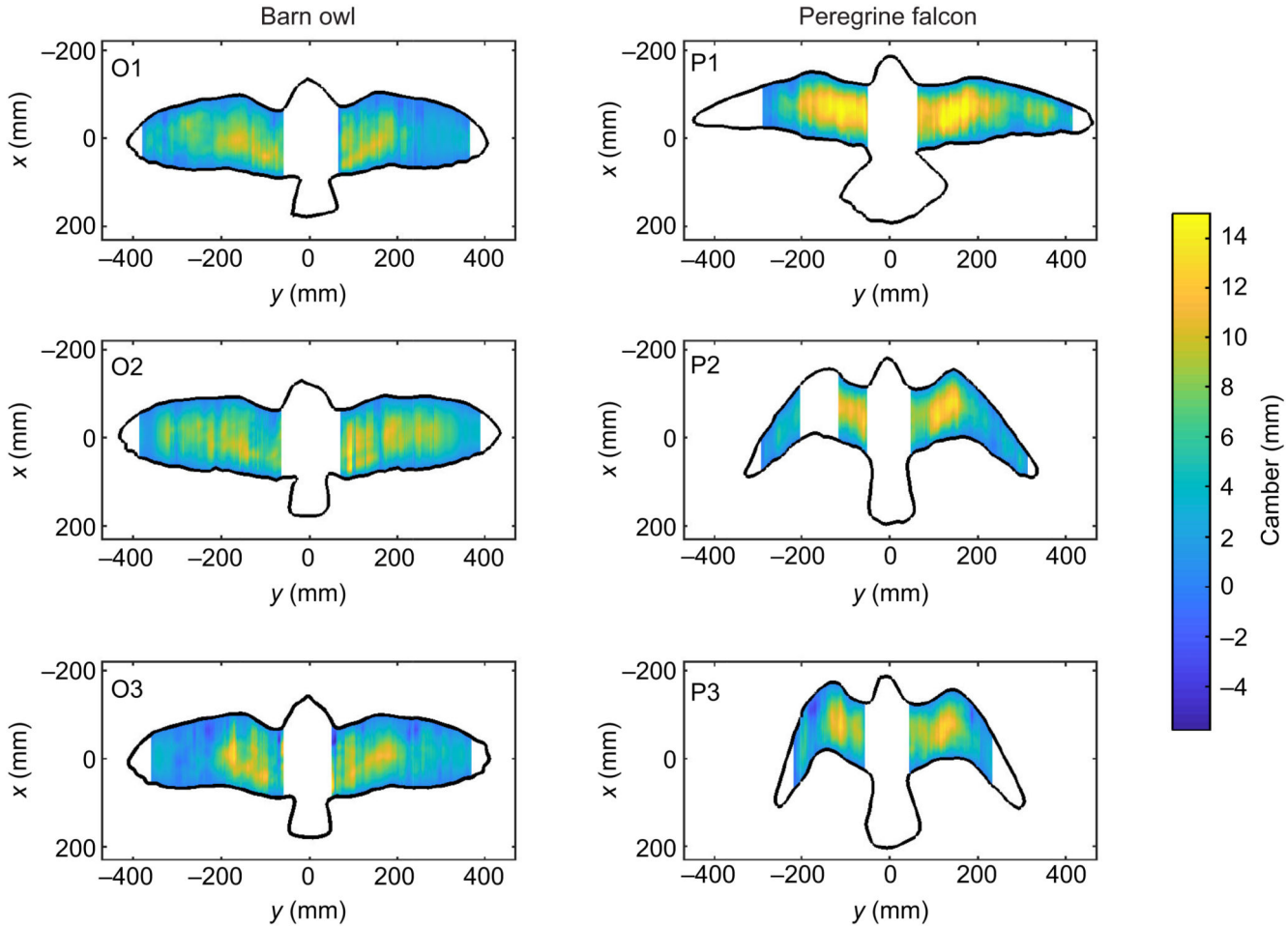

Fig. 7. Camber distribution for each flight.

Scalar fields quantifying the distance between the mean camber line and chord line, as measured perpendicular to the chord line, for sections every 2 mm along the span for the barn owl (O1–O3) and peregrine falcon (P1–P3) flights. Uncoloured regions represent the body, tail and regions with reduced data quality (i.e. near the wing tips) or where linear fitting was used to generate the mean camber line (see Fig. S3). Camber distribution normalised by the local chord length showed a very similar distribution, both between flights and between birds.

Europe PMC Funders Author Manuscripts

Europe PMC Funders Author Manuscripts

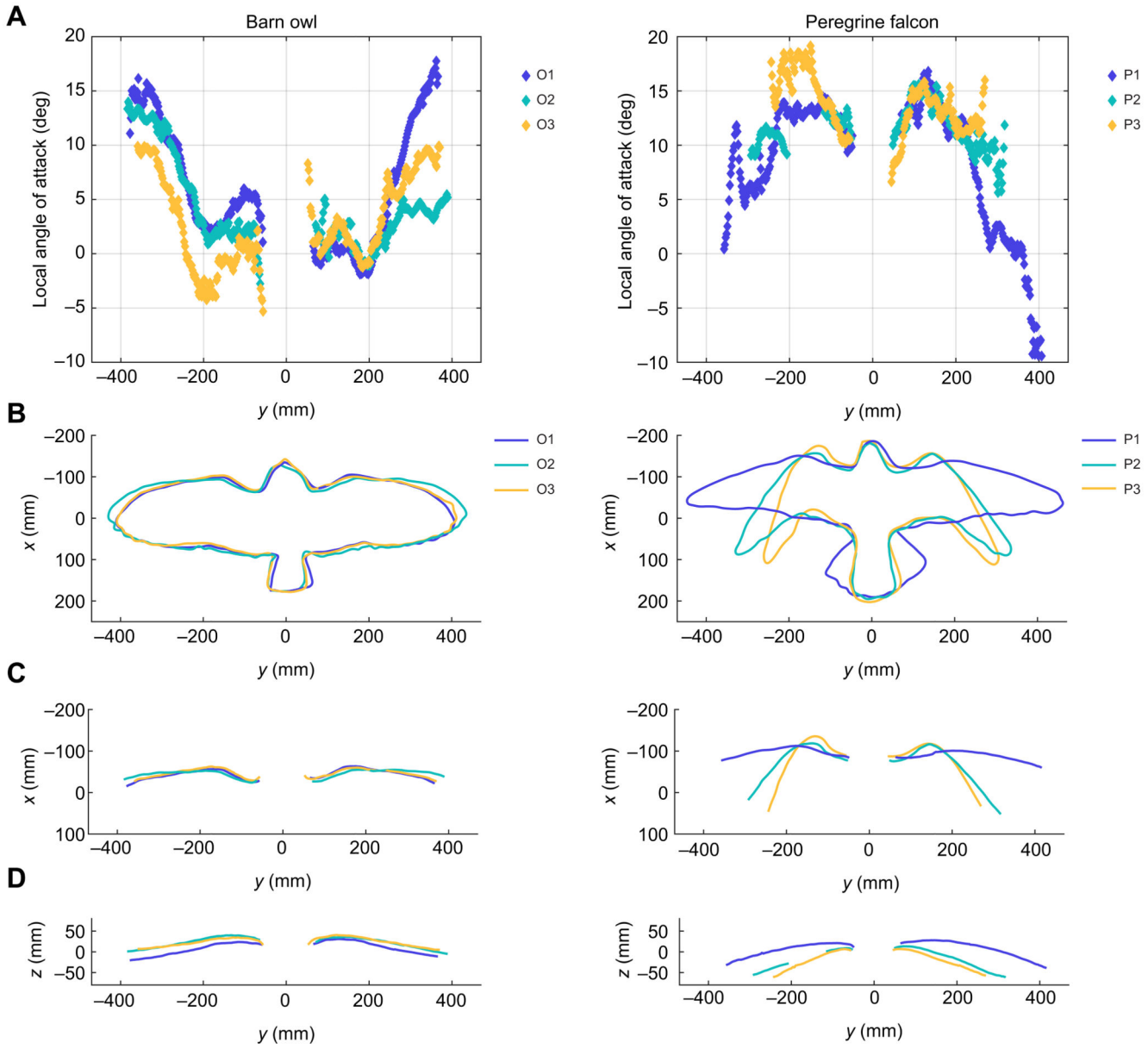

Fig. 8. Geometric data for each flight.

(A) Spanwise angle of attack. (B) Planform outline showing the overall wing and tail configuration. (C) Dorsoventral view of the quarter-chord, showing wing sweep. (D) Posteroanterior view of the quarter-chord, showing wing dihedral.

Table 1

Flight data derived from the geometry, video and anemometer data for the barn owl (O1–3) and peregrine falcon (P1–3) flights

	Barn owl			Peregrine falcon		
	O1	**O2**	**O3**	**P1**	**P2**	**P3**
Mass (g)	312	312	312	645	645	645
Wing span (mm)	818	864	820	908	666	562
Mean aerodynamic chord (mm)	126	129	128	102	102	109
Wing area (m^2)	0.117	0.126	0.118	0.103	0.081	0.076
Aspect ratio	5.7	5.9	5.7	8.0	5.5	4.2
Wing loading ($N\ m^{-2}$)	26.2	24.3	25.9	61.4	78.1	83.3
Ground speed ($m\ s^{-1}$)	6.3±0.2	6.0±0.2	6.7±0.2	8.6±0.3	9.7±0.4	10.6±0.4
Wind speed ($m\ s^{-1}$)	2.6±0.4	3.1±0.5	1.7±0.5	1.4±0.4	2.6±0.4	4.0±0.9
True air speed ($m\ s^{-1}$)	8.7±0.6	8.9±0.7	8.3±0.7	9.6±0.7	12.0±0.8	14.4±1.3
Mean wing angle of attack (deg)	6.1±3.6	4.3±2.3	2.9±1.8	8.1±1.9	11.5±1.8	13.7±1.5
Tail angle of attack (deg)	20.7±3.6	28.5±2.3	17.8±1.8	24.2±1.9	18.6±1.8	19.1±1.5
Mean corrected longitudinal dihedral (deg)	−9.6	−19.2	−9.9	−11.1	−2.1	−0.4
Tail twist (deg)	−4.7	12.6	−5.2	11.0	−0.3	5.1
Angle of sideslip (deg)	−3.8±4.2	8.3±3.8	2.6±2.8	5.7±1.8	5.1±2.6	−3.9±1.9
Lift coefficient	$0.6^{+0.09}_{-0.07}$	$0.53^{+0.08}_{-0.07}$	$0.65^{+0.13}_{-0.10}$	$1.15^{+0.19}_{-0.15}$	$0.94^{+0.14}_{-0.11}$	$0.69^{+0.13}_{-0.10}$
Roll attitude (deg)	1.9	6.5	8.7	2.3	1.8	−2.4
Altitude (m)	1.34	1.35	1.31	1.27	1.30	1.10
Altitude loss (mm)	9	62	−40	214	227	229
Glide angle (deg)	0.25	1.7	−1.0	5.3	5.9	5.4

Data are means±s.d. except ground speed where the error was based on ±1 frame in the video footage used in its estimation. Differences in upper and lower bounds of the lift coefficient errors are due to the V^2 term in the lift equation. All estimates of s.d. were based on the anemometer measurements of wind velocity over a 5 s period (n=20).

Europe PMC Funders Author Manuscripts

Table 2

Stated error for surface measurements of flying birds obtained from other methods

Reference	Stated error	Resolution
Butz et al. (1985)	Range: ±0.3 mm at distance 800 mm	Low
Carruthers et al. (2010)	Absolute μ=4.31 mm	Low
Wolf and Konrath (2015)	σ<0.3 mm at distance 1400 mm	High
Deetjen et al. (2017)	μ=0.31 mm, σ=1.03 mm	High
Present results	μ=−0.016 mm, σ=1.31 mm	High

The error (μ, mean; σ, s.d.) for the present results is based on individually aligned reconstructions without the edges removed as this was most comparable to the other methods.